Pre-eruptive timescales from the historical Hapaimamo eruption at Mauna Loa, Hawai'i

F.K. Couperthwaite [a,c,*], D.J. Morgan [a], J. Harvey [a], M. Kahl [b]

[a] School of Earth and Environment, University of Leeds, Leeds LS2 9JT, UK
[b] Institute of Earth Sciences, Heidelberg University, Heidelberg 69120, Germany
[c] College of Earth, Ocean and Atmospheric Sciences, Oregon State University, Corvallis, Oregon, 97331, USA

ARTICLE INFO

ABSTRACT

The 240 yr B.P. Hapaimamo eruption occurred on the southwest rift zone (SWRZ) of Mauna Loa. A large tephra deposit and an extensive lava flow field were produced that extend from 1880 m above sea level down to the southwest coast. Detailed petrological study of olivine crystals from both deposit types are used to determine the timescales of crystal disaggregation from a cumulate mush zone. Over 70% of studied olivines in both, lava flow and tephra samples, exhibit normal zoning. Tephra and flow olivine core compositions are between Fo_{89-84} and Fo_{89-81}. Olivine rims in the tephra have compositions of Fo_{86-81}, whereas rims in the flow samples extend to lower values within the range Fo_{83-71}. The remaining tephra olivines are unzoned and fall within the same core compositional range. Using Fe—Mg interdiffusion chronometry, we calculate tephra olivine diffusion timescales from 13 to 1600 days (days to years), with over 70% of timescales <100 days, and lava flow olivine diffusion timescales from 25 to 1110 days with 65% of timescales >100 days. Zoning widths were defined as narrow (type I) or broad (type II) and together with the diversity of timescales indicate an ongoing process of crystal mush disaggregation into the erupted host melt.

Comparison of tephra and flow diffusion timescales show consistently longer timescales across the lava flow population, as expected due to continued diffusive re-equilibration. Our results suggest that where textural evidence allows, and tephra timescales can be compared, olivines from lava flows can be used to provide temporal information for magmatic processes within the subsurface and the lava flow. Comparison of published elemental diffusion timescales between Mauna Loa and neighbouring Kīlauea suggest that magma mobilisation and transfer processes occur over similar timescales within the plumbing systems of both Mauna Loa and Kīlauea.

1. Introduction

Despite being the larger of the active volcanoes that comprise the Island of Hawai'i ("Big Island"), Mauna Loa is less well-understood than neighbouring and more frequently-active Kīlauea Volcano which sits to the southeast. With only two eruptive episodes (1975 and 1984) since the installation of permanent seismic and deformation monitoring networks in the 1950s and 1960s, there are far fewer geophysical observations available than for Kīlauea Volcano. Historical Mauna Loa eruptions between 1843 and 1950 occurred largely unmonitored by modern standards (Poland et al., 2014). The relatively sparse data allow quite generalised geophysical modelling but not to the detail available for Kilauea; there is therefore the need to better understand the nature and dynamics of Mauna Loa's plumbing system via studying erupted products of past eruption cycles.

From the summit caldera Moku'āweoweo, two rift zones extend towards sea level; the northeast rift zone (NERZ) and the southwest rift zone (SWRZ) (Lockwood and Lipman, 1987; Barnard, 1995; Garcia et al., 1995). Geophysical modelling suggests the presence of a summit reservoir located at 3–4 km depth towards the south east of the caldera (Decker et al., 1983; Okubo et al., 1997; Poland et al., 2014); in parallel, geochemical studies have proposed a model for Mauna Loa lavas whereby lavas originate from "a shallow, long lived, continuously replenished and homogenized magma reservoir" (Rhodes, 1988; Rhodes, 1995). In addition to the shallow summit reservoir located at ~3–4 km, a much deeper reservoir at 7–8 km has also been suggested (Rhodes, 1988; Decker et al., 1983; Poland et al., 2014). Other authors have proposed the possibility of isolated storage areas beneath the rift zones,
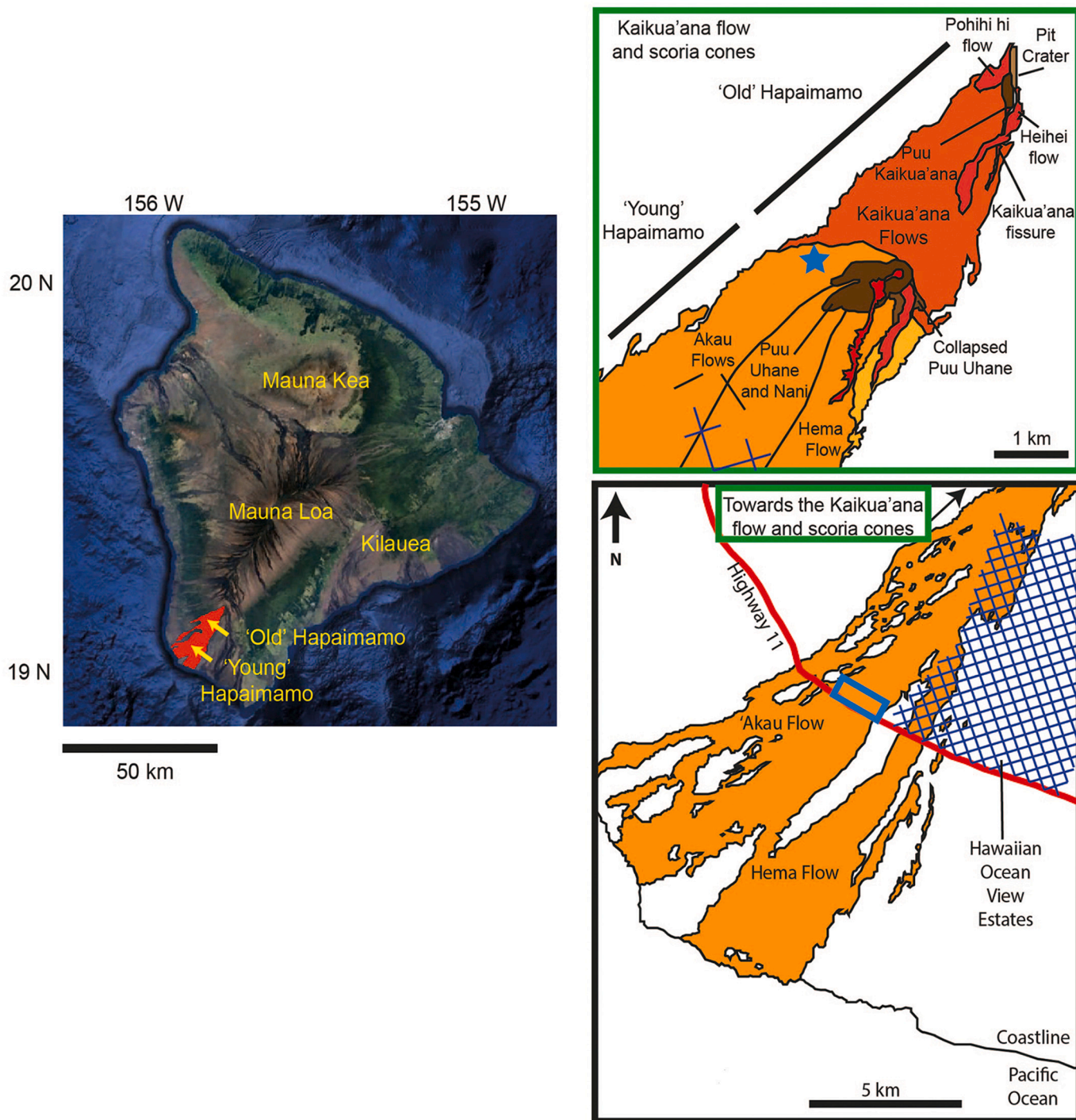
Fig. 1. *Location map of the Hapaimamo flow on the southwest rift zone (SWRZ) of Mauna Loa, Big Island, Hawai'i.* Google earth image showing the position of the Hapaimamo eruptive deposits on the SWRZ. The schematic diagram outlined in black illustrates the boundaries of the younger 'Akau and Hema flows and the location of the road cut sampled for this study (blue box). Highlighted in green, are the source vents and the relationship of the younger flows related to the older Kaikua'ana flow. Also highlighted is the sampled tephra site (blue star). Map adapted from Tsang et al. (2008), Müeller, (2005) and Garcia and Chapman (2012). (For interpretation of the references to colour in this figure legend, the reader is referred to the web version of this article.)

evidenced by the diversity of incorporated xenolith compositions that would not be consistent with a large, steady-state magma chamber (Gaffney, 2002) and the presence of mafic erupted magmas that have avoided the buffering effects of evolved magma in the shallow summit magma chamber (Garcia et al., 1995). These studies therefore suggest a degree of complexity in the nature and extent of subsurface magma storage and transport.

A rather new aspect is time, which is critical when assessing the evolution of magma storage, accumulation, interaction and mobilisation. These processes can occur over days to weeks up to years before eruption. Time can be constrained by modelling the diffusion of chemical heterogeneities in minerals. Diffusion chronometry has become an integral tool for constraining the timescales of magma residence, mixing and transport prior to eruption (e.g. e.g. Costa et al., 2003; Morgan and Blake, 2006; Kahl et al., 2011; Saunders et al., 2012; Kahl et al., 2013; Shea et al., 2015; Rae et al., 2016; Lynn et al., 2017, Ruth et al., 2018;
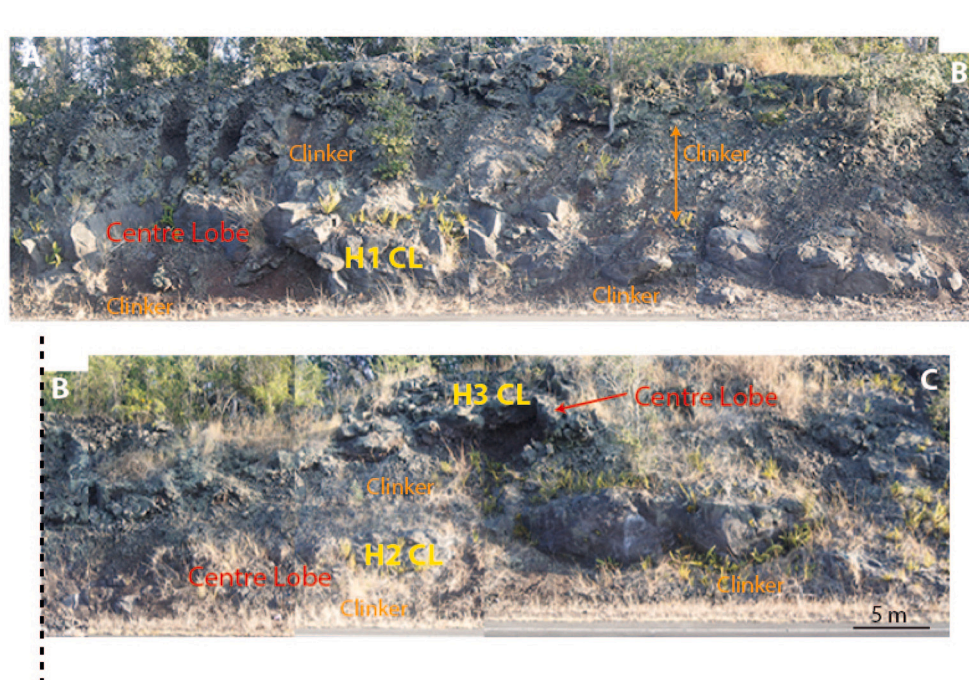
Fig. 2. *Annotated photograph of the road outcrop of the Hapaimamo lava flow.* Central lobes and top and basal crust ('clinker') are highlighted in red and orange respectively. Sample sites for H1, H2 and H3 centre lobe are indicated in yellow. The images are one continuous road outcrop, separated into two images at the black dashed line. (For interpretation of the references to colour in this figure legend, the reader is referred to the web version of this article.)

Rasmussen et al., 2018; Mutch et al., 2019a, 2019b; Caracciolo et al., 2021; Mutch et al., 2021). Despite the abundance of eruptive products along Mauna Loa's rift zones, there exists at present no coherent record concerning the timescales of sub-surface magma mobilisation and transfer (e.g., Couperthwaite et al., 2020).

In this contribution, we report whole-rock data of tephra and lava flow samples from an early stage of the 240 yr B.P. (Trusdell and Lockwood, 2020) Hapaimamo eruption at Mauna Loa, linked with results of olivine (Fe—Mg) interdiffusion chronometry to constrain pre-eruptive timescales of mush disaggregation and magma mobilisation. Parallel study of both tephra (rapidly quenched) and lava flow samples (more slowly-quenched) from the same eruption allows the extent to which diffusion timescales have been affected by diffusive re-equilibration during lava flow emplacement to be constrained. This then enables comparison of olivine Fe—Mg interdiffusion timescales calculated to date from Mauna Loa with the results of previous studies of Kīlauea products (Rae et al., 2016; Lynn et al., 2017; Bradshaw et al., 2018) to assess similarities or differences in behaviours and dynamics between the two magmatic systems.

2. Regional setting of the Hapaimamo products

The Hapaimamo vent and flow field is located on the lower slopes of the Southwest Rift Zone (SWRZ), dated via radiocarbon (^{14}C) dating to an age of ~240 ± 60 years B.P. from charcoal at the base of a flow (Trusdell and Lockwood, 2020). The flow field covers an area of 95.6 km^2 with an estimated volume of 468×10^6 m^3 giving an average thickness of 4.9 m, making it one of the largest flows on Mauna Loa's SWRZ (Müller, 2005; Garcia and Rhodes, 2012). Müller (2005), distinguishes three main subunits within the flow that can be further subdivided into "old" and "young" Hapaimamo based on relative age, using stratigraphic relationships and spatial distribution. These are, in sequence the Kaikua'ana flow, the 'Akau flow and the Hema flow (all informal names; Fig. 1). Compositionally, all are basaltic, though the later parts of the Hema flow also contain picrites with 15–50% modal olivine. The samples for this study are taken from a roadcut through the

Table 1
Field summary of lava flow samples.

Sample Name	Coordinates (UTM Zone 5Q)	Description
Hapaimamo Tephra	0209477E 2122694N	Reticulite, Golden in colour. Abundant olivine.
H1 (blocky lava core with top and bottom clinker)	0203453E 2114908N	Lava core ~1.5–2 m thick. Increase in vesiculation towards the top. ~15% olivine 2 mm – 1 cm in size, evenly distributed. Xenoliths ~2 cm present in the lower section
H2 (blocky lava core with top and bottom clinker)	0203471E 2114890N	Taken from the same lobe as H1 ~25 m to the east. Lava core ~1 m thick. Abundant olivines 2 mm – 1 cm in size. Xenoliths present.
H3 (blocky lava core with top and bottom clinker)	0203480E 2114895N	Taken from a separate lobe ~2 m above H1 and H2. Lava core ~1 m thick. ~10% olivine evenly distributed. Grading of vesicles towards the top of the unit.

'Akau flow (the lower part of the "young" Hapaimamo) and its associated tephra within Kahuku section of the Hawaii Volcanoes National Park. Full details of the reconstructed eruption chronology and the sequence of vent opening and emplacement are given by Müller (2005).

3. Material and methods

3.1. Sampling and field observations

A reticulite tephra sample was taken from the scoria cone deposits to the north of the Hawaiian Ocean View Estates within Kahuku Ranch (blue star, Fig. 1). This tephra was sampled near the vent (< 1 km away) alongside the road that runs through Kahuku Ranch, highlighted on Fig. 1. Here the deposit is ~2 m thick forming an extensive reticulite field. Each clast is 3–4 cm in size and can contain 2 or 3 olivine crystals, commonly visible with the naked eye and encased within layers of volcanic glass.

Lava flow samples were collected from the 'Akau flow along a road cut, also highlighted in Fig. 1 (blue rectangle). Three sets of samples were collected from different flow lobes. Each sample set consists of the blocky core or central lobe with a clinker crust above and below (where clinker is the smaller, rubble fragments) sampled through a vertical section of each lobe. Sample names are denoted H1, 2 or 3 and TC for top clinker, CL for centre lobe or BC for basal clinker. Olivine crystals are denoted by letters, and microprobe traverses within those crystals by numbers (i.e., H1CL_A1 is the first traverse in olivine crystal A from the core lobe sample of the lobe H1). Fig. 2 shows the sample locations and examples in the field outcrop of the terminology used. A brief description of each sample can be found in Table 1.

H1 and H2 were sampled from the same lava flow lobe but from laterally different sections. H3 was sampled from a flow lobe emplaced later in the eruption sequence and is part of the same flow field. Those parts of the 'Akau flow that were sampled are characterized as "proximal 'a'ā" following the definition of Rowland and Walker (1987). Proximal 'a'ā is defined as being 1–3 m thick, with thin layers of spiny clinker with fine material mixed in, and lobes often have vesicular interiors. Each of the Hapaimamo sheets is up to 3 m thick from the basal clinker through the flow core (~1.5 m thick) to the upper clinker. H3 follows the landscape with the same general structures as H1/H2, however it has a thinner interior core, ~0.5 m. The interior cores are weakly vesiculated (~4–16%) containing olivines up to 3 mm in size. The flows are olivine phyric containing ~5–15 vol%. Xenoliths of dunite (olivine only) and harzburgite (olivine + orthopyroxene) measuring ~1 cm in diameter are also present.

3.2. Sample preparation

The tephra was carefully hand crushed, and individual olivines or olivine clusters ranging in size from 5 mm to 250 μm were picked and separated by size. The olivine crystals were mounted in resin blocks, ground and polished, using colloidal silica for a final polish to create a flat surface exposing each crystal for imaging.

For the lava flow, we focused on preparing material from the core of the flow, as the clinker material was heavily oxidized, and therefore unsuitable for diffusion studies. Standard thin sections were prepared for each sample (H1,H2,H3), ground and polished following the methods used for the tephra crystal blocks.

3.3. Analytical methods

3.3.1. X-ray fluorescence (XRF)

Bulk-rock major element analyses for sample H2 were determined by x-ray fluorescence (XRF) at Origin Analytics, Welshpool using a 4KW Bruker S4 WD-XRF instrument. Samples were prepared as fused disks using a Claisse M4 fusion instrument; 0.5000 g ± 0.0005 g of sample was combined with 7.5000 g $\pm$ 0.0005 g of flux (50:50 mix of $Li_2B_4O_7$: $LiBO_2$) and fused using the Claisse default program 3 before being poured into 32 mm casting dishes. The machine was calibrated using 25 geological reference materials prepared in an identical manner to the samples. Drift was monitored using the Ausmon drift correction standard (XRF Scientific Ltd) and corrected within the instrument software. Loss on ignition was determined gravimetrically on a separate powder aliquot after heating to $1025\ ^{\circ}$C. To test the accuracy and reproducibility of the data collected, the published values for KH03-10 L basalt measured at the The Open University (Harvey et al., 2012) were compared to re-analysed values of this sample by Origin Analytics with the Hapaimamo samples. The *relative* percentage differences between the two measurements of KH03-10 L are 0.1–1.4% for SiO_2, Al_2O_3, Fe_2O_3, MnO, MgO, CaO, K_2O and P_2O_5 and 2.8 and 2.9% for CaO and TiO_2 respectively.

Bulk-rock major element analyses for lavas samples H1 and H3 and the tephra sample were determined by XRF at the University of Edinburgh, using a Panalytical PW2404 wavelength-dispersive sequential x-ray spectrometer. Three USGS standards (BHVO-1, STD-BEN and STD-BCR) were analysed alongside the Hapaimamo samples at the University of Edinburgh for precision and accuracy. For each standard, 1sigma errors of <0.05 wt% *absolute* were reported for all major elements. The techniques used are similar to those described by Fitton et al. (1998) with modifications given by Fitton and Goddard (2004) as reported in Hartley and Thordarson (2013). All XRF data and uncertainties can be found in Supplementary Data.

3.3.2. Scanning electron microscopy

High resolution backscattered electron (BSE) images of olivine blocks and thin sections were collected for textural assessment and for composition calibration for diffusion modelling using an FEI Quanta 650 FEG-ESEM Scanning Electron Microscope (SEM) at the University of Leeds Microscopy and Spectroscopy Centre (LEMAS). The imaging was conducted using an accelerating voltage of 20 kV.

3.3.3. Electron backscatter diffraction (EBSD) analysis

An Oxford Instruments electron backscatter diffraction system (EBSD, Prior et al., 1999) equipped with *hkl Systems Nordlys* detector was used to acquire orientation data of the crystallographic a-, b-, and c-directions in olivine using the FEI Quanta 650 FEGSEM at LEMAS. EBSD patterns were processed using Oxford Instruments *Channel 5* software giving a single set of Euler angle rotations per grain. These were used to calculate crystallographic orientations relative to the EBSD analytical plane. This allows us to correct for the strongly anisotropic interdiffusion of Fe—Mg in olivine (Dohmen and Chakraborty, 2007a, 2007b; Dohmen et al., 2007).

3.3.4. Electron microprobe analysis (EMPA)

Compositional rim-to-core traverses of olivine grains were measured using a JEOL JXA8230 Electron Microprobe (EMP) equipped with five wavelength-dispersive spectrometers (WDS) at LEMAS. We retrieved 91 compositional profiles for Fe—Mg diffusion modelling. Where possible, more than two profiles were analysed from the same crystal slice at different orientations. Compositional traverses perpendicular to the crystal edge were analysed with a focused beam at 5–10 μm intervals. The dataset was collected over multiple runs using slightly different beam conditions (15–20 kV and a beam current of 40–50 nA) and on-peak count times were as follows; 40 s for Si, Fe and Mg, and 60 s for Ni and Mn. Analyses with totals <98.5 and > 101.2% were discarded. Microbeam reference materials distributed by the Smithsonian Institute, Washington D.C. (Jarosewich et al., 1980) were used as primary standards and detection limits are reported in the Supplementary Data. Repeated analyses of the San Carlos olivine standard were used to calculate the external accuracy and reproducibility of the olivine compositions via analyses at the start, end and within-run. The Fo (Mg/Mg + Fe) content of the San Carlos olivine was reproducible within-run precisions of $2\sigma = 0.05$–0.14 mol% ($n = 66$ over the course of the study). All olivine compositions are provided in the Supplementary Data. Analyses of groundmass minerals within the lava flow were conducted alongside suitable matrix-matched standards, as detailed in the Supplementary Data.

To collect compositional data of tephra matrix glasses and olivine-hosted melt inclusions, the beam current was lowered to 10 nA and measured using a defocused beam of 10 μm to minimise ionic mobility of elements such as Na during analysis (Morgan and London, 1996). The following on-peak count times were used; 24 s for Mg and Ti, 30 s for P, 20 s for Mn, Fe, Ni and Cr, and 10s for Ca, Al, Na, K and Si. Totals <97 and > 101.2% were discarded. Detection limits and primary standards are detailed in the Supplementary Data. Two or three spot analyses were taken per melt inclusion, resulting in a total of 61 melt inclusion analyses. Where 2 analyses of a melt inclusion are the same composition, we use the average, for further analysis. Only melt inclusions >30 μm in diameter and located towards the apparent centre of an olivine free of cracks were analysed to avoid inclusions that may have retained

Table 2

Selected glass compositions (Uncorrected and corrected melt inclusions compositions and matrix glass compositions).

	SiO$_2$	TiO$_2$	Al$_2$O$_3$	Cr$_2$O$_3$	FeO	NiO	MnO	MgO	CaO	Na$_2$O	K$_2$O	P$_2$O$_5$	TOTAL
					Oxide wt%								
Uncorrected MI													
Block 2_Ba_MI1	53.86	1.73	13.45	0.03	10.18	0.01	0.13	6.72	10.48	2.19	0.26	0.23	99.28
Block 2_Ba_MI1	53.78	1.69	13.38	0.06	10.14	−0.02	0.16	6.68	10.39	2.16	0.26	0.21	98.91
Block 2_Ba_MI1	54.11	1.75	13.31	0.05	10.24	0.01	0.19	6.74	10.43	2.19	0.26	0.19	99.48
Block 2_Bb_MI2	53.81	1.9	13.58	0.04	10.13	0.03	0.16	6.76	10.49	2.18	0.39	0.3	99.76
Block 2_Bb_MI2	53.28	1.9	13.78	0.02	9.99	0.01	0.14	6.72	10.43	2.26	0.4	0.29	99.23
Block 2_Bb_MI2	53.46	1.92	13.66	0.04	10.17	0.01	0.18	6.78	10.53	2.21	0.4	0.27	99.63
Block 2_D_MI3	55.14	1.85	14.49	0.04	6.87	0.01	0.11	6.89	10.62	2.36	0.35	0.2	98.94
Block 2_D_MI3	55.34	1.86	14.47	0.06	6.83	0.01	0.12	6.83	10.75	2.43	0.35	0.2	99.26
Block 2_E_MI4	52.62	1.74	14.34	0.06	8.42	0.03	0.11	7.28	11.74	2.03	0.33	0.18	98.88
Block 2_E_MI4	52.74	1.75	14.33	0.05	8.41	0.04	0.13	7.35	11.65	1.89	0.31	0.18	98.84
Block 2_F_MI5	55.49	1.84	14.42	0.24	7.49	0.03	0.14	6.64	10.55	2.16	0.35	0.23	99.58
Corrected MI													
Block 2_Ba_MI1	52.76	1.6	12.42	0.04	10.59	0.03	0.14	9.62	9.69	2.02	0.24	0.21	99.35
Block 2_Ba_MI1	52.7	1.56	12.31	0.06	10.56	0.01	0.17	9.74	9.58	1.99	0.24	0.19	99.1
Block 2_Ba_MI1	53.13	1.63	12.43	0.05	10.63	0.03	0.19	9.25	9.74	2.05	0.24	0.18	99.56
Block 2_Bb_MI2	52.67	1.74	12.47	0.04	10.54	0.05	0.16	9.86	9.65	2	0.36	0.28	99.82
Block 2_Bb_MI2	52.23	1.76	12.72	0.02	10.41	0.03	0.15	9.67	9.65	2.08	0.37	0.27	99.35
Block 2_Bb_MI2	52.34	1.77	12.57	0.04	10.57	0.03	0.18	9.83	9.7	2.03	0.37	0.25	99.69
Block 2_D_MI3	54.57	1.78	13.93	0.04	7.08	0.02	0.11	8.46	10.22	2.27	0.34	0.19	99.01
Block 2_D_MI3	54.72	1.78	13.87	0.06	7.05	0.03	0.12	8.49	10.31	2.33	0.33	0.19	99.29
Block 2_E_MI4	51.45	1.58	12.96	0.06	8.76	0.06	0.12	11.12	10.63	1.83	0.3	0.17	99.04
Block 2_E_MI4	51.65	1.6	13.09	0.05	8.74	0.07	0.14	10.83	10.66	1.73	0.28	0.16	98.99
Block 2_F_MI5	54.43	1.71	13.46	0.23	7.81	0.05	0.14	9.31	9.85	2	0.33	0.22	99.54
Matrix glass													
Block 2_K	52.46	1.96	13.89	0.03	10.77	0.03	0.18	6.85	10.67	2.28	0.38	0.21	99.72
Block 2_K	51.96	1.98	13.92	0.05	10.73	0.03	0.15	6.84	10.69	2.23	0.37	0.22	99.17
Block 2_K	52.25	1.95	13.61	0.05	10.77	0.01	0.15	6.83	10.58	2.22	0.36	0.23	99.02
Block 2_K	52.17	1.95	13.77	0.02	10.71	0.02	0.16	6.83	10.66	2.27	0.37	0.22	99.15
Block 2_K	52.26	1.96	13.82	0.02	10.83	0	0.18	6.81	10.65	2.22	0.37	0.24	99.38
Block 2_K	52.15	1.92	13.9	0.04	10.74	0	0.16	6.86	10.54	2.27	0.39	0.22	99.2
Block 2_K	51.94	1.95	13.73	0.06	10.81	0.02	0.19	6.8	10.55	2.25	0.37	0.24	98.91
Block 2_K	52.56	1.95	13.75	0.06	10.72	−0.24	0.16	6.87	10.83	2.23	0.38	0.23	99.51
Block 3_A	52.24	1.98	13.7	0.04	10.66	0.01	0.16	6.76	10.55	2.21	0.4	0.22	99.22
Block 3_A	52.15	1.98	13.91	0.04	10.66	0.02	0.17	6.68	10.73	2.25	0.4	0.22	99.61
Block 3_A	52.42	1.95	13.92	0.04	10.84	0.03	0.15	6.79	10.67	2.16	0.38	0.25	100.35
Block 3_A	52.98	1.97	14.15	0.05	10.8	0.02	0.14	6.81	10.58	2.22	0.38	0.24	99.5

connection to the external melt.

3.4. Post-entrapment crystallisation correction of melt inclusions

Melt inclusions can be significantly modified by post-entrapment processes such as crystallisation of olivine on the walls of the inclusion known as post-entrapment crystallisation (PEC; Sisson and Layne, 1993; Kress and Ghiorso, 2004; Humphreys et al., 2008), where this process leads to a net decrease in Fe content of the melt inclusion (Danyuchevsky et al., 2000). Within the tephra olivine, we corrected the composition of melt inclusions using the Petrolog3 software (Danyuschevsky and Plechov, 2011). For this calculation, Petrolog3 requires input of the initial FeO$_T$ of the melt inclusions. We calculated the initial FeO$_T$ using the method of Wieser et al. (2021), as the liquid line of descent for Mauna Loa glasses is very similar to that for Kīlauean glasses (Supplementary Materials). This method uses a constant FeO$_T$ composition. Our estimate for the initial FeO$_T$ contents of the tephra olivine inclusions is ~10.7 wt% (compared to 11.3 wt% for melt inclusions from olivines of the 2018 Kīlauea eruption). Further details of the methodology and the Petrolog3 model parameters can be found in the Supplementary Materials. Representative melt inclusion compositions (both corrected and uncorrected) are shown in Table 2. Fully recrystallised melt inclusions were not analysed.

4. Results

4.1. Petrography

Olivine is the most abundant mineral phase (estimated at >90%) found in the tephra and lava samples with lower abundances of clinopyroxene and plagioclase (each estimated at <5% of crystals picked). In the tephra, neither the olivine-hosted melt inclusions nor the matrix glasses contain microlites. In the lava flow groundmass, plagioclase is present with an estimated modal abundance of ~50%, often ~50 μm in size. All plagioclase crystals are lath or brick shaped and are unzoned, with core values of An$_{69-66}$. Clinopyroxene crystals are present in the groundmass with an estimated modal abundance of ~50%. Clinopyroxene frequently preserve a uniform rim ~20–40 μm in width. Clinopyroxene crystals show complex zoning often with resorption textures. The core compositions have (Mg/(Mg + Fe)x100) = 81–76 and Ca/(Ca + Mg + Fe) = 0.41–0.34.

The oxides in the groundmass are chromium-spinel (with an average Cr (Cr/Cr + Al) number of 0.50) and titanomagnetite (with an average ulvospinel component of 0.61). The oxides altogether make up less than 5% of the modal crystal abundance. No olivine crystals are found in the groundmass.

4.2. Whole rock geochemistry

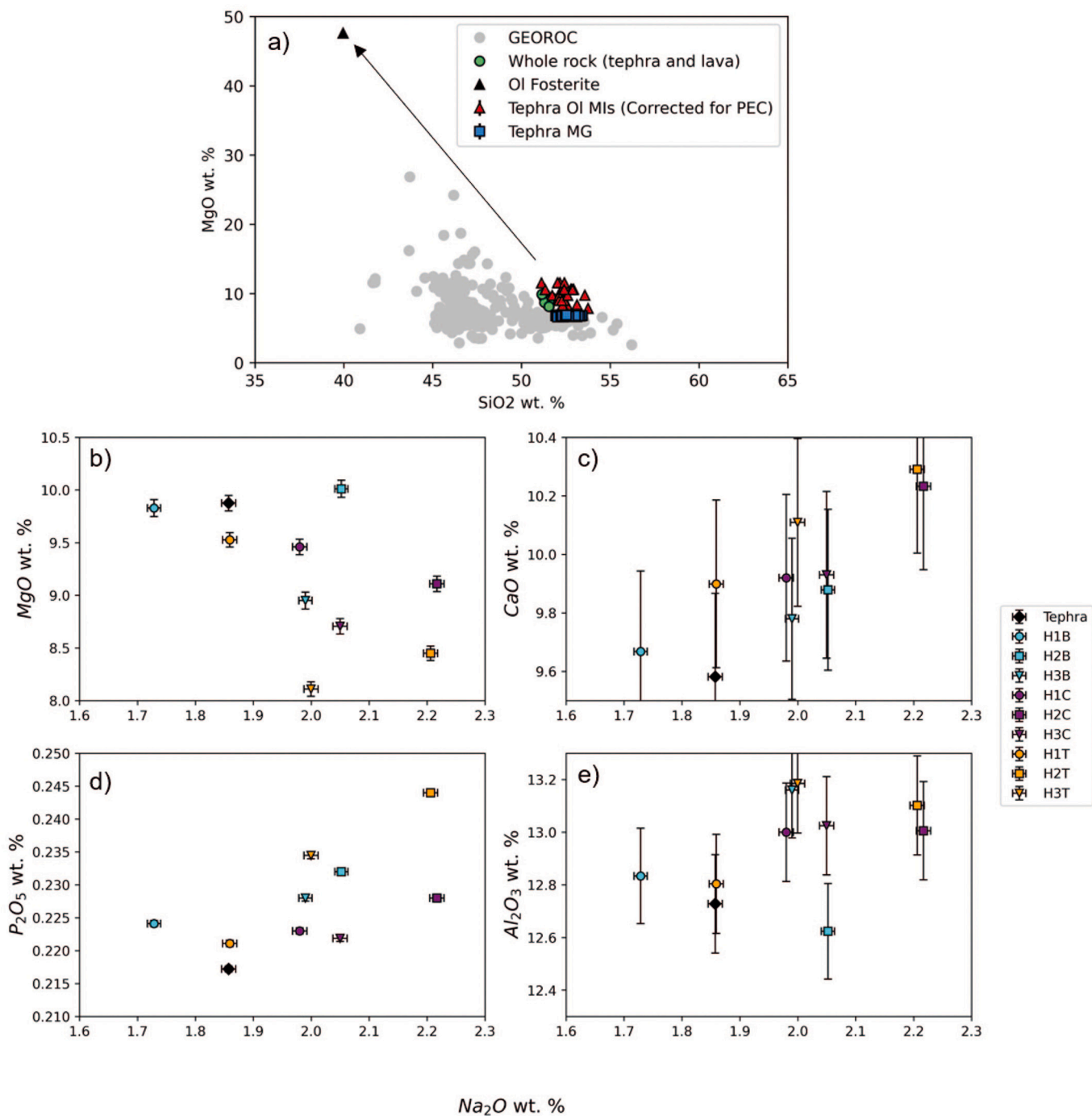Whole rock compositions plot towards the higher MgO (>8 wt%

Fig. 3. *Whole rock compositions and Na$_2$O variation diagrams of the tephra and lava flow* (a) MgO vs. SiO$_2$ plot of whole rock (tephra and lava), matrix glass (tephra) and PEC-corrected olivine-hosted melt inclusion (tephra) compositions. Grey filled circles: Compilation of Hawaiian whole rock compositions from the GEOROC database (http://georoc.mpch-mainz.gwdg.de/georoc/) for comparison. Black triangle: average forsterite composition of olivine (Fo$_{87}$). Olivine control line indicating that the compositional fractionation is controlled by the addition of olivine. (b-d) Major element vs. Na$_2$O plots of whole rock compositions of the 'Akau tephra and lava flow samples. Error bar: 1 sigma.

MgO), lower SiO$_2$ (<52 wt% SiO$_2$) range of Hawaiian basalts (Rhodes, 1983; Rhodes, 1995; Fig. 3a). The 'Akau flow and tephra and older Kaikua'ana flows are very similar in composition (Müller, 2005) (see Supplementary Materials) and there is little range in the major element compositions of the 'Akau tephra and lava flow samples (Fig. 3b-e). There is a broad negative covariation of MgO with Na$_2$O and slightly higher MgO towards the base of flows than the top. This could be linked to the abundance of olivine and settling of olivine crystals. The tephra compositions lie towards the more primitive lava compositions.

The relative homogeneity of the 'Akau flow and tephra samples are consistent with the findings of Rhodes (1983 and 1995) who observed that most historical Mauna Loa lavas are homogeneous in composition, though Müller (2005) notes that the Hapaimamo eruption becomes more picritic in the uppermost, later Hema flow (Müller, 2005), which is not part of this study.
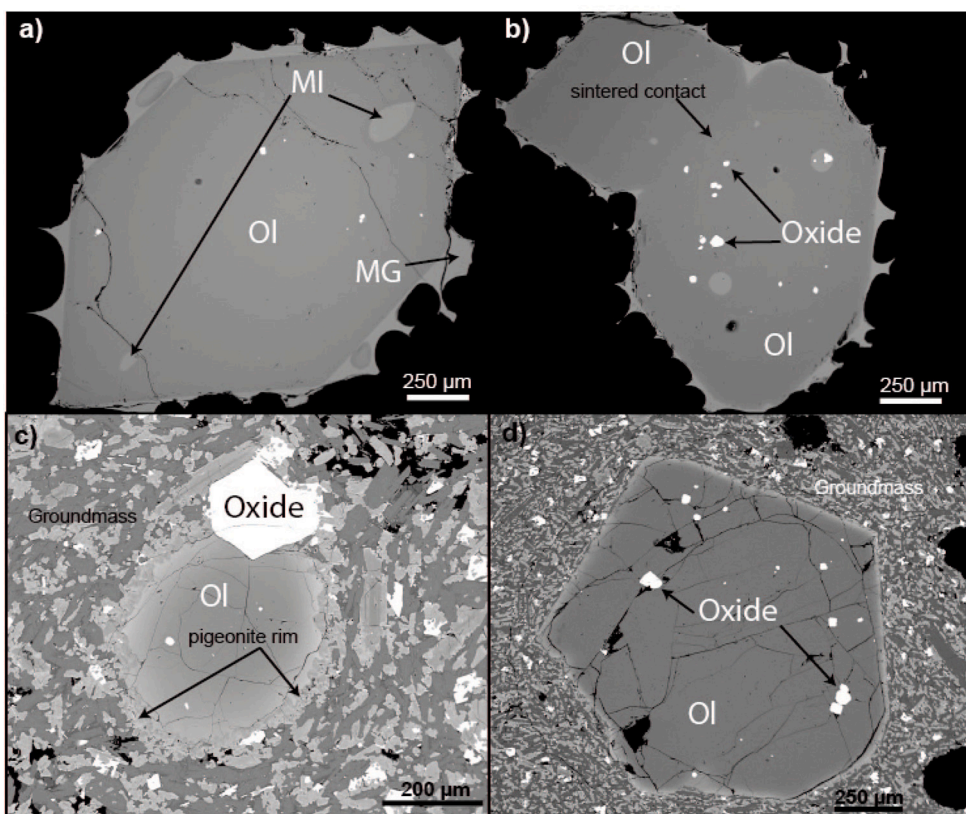
Fig. 4. *Backscattered electron (BSE) images of olivines within the tephra and lava flow samples* a) Euhedral tephra olivine crystal containing naturally quenched melt inclusions. b) A pair of olivines from the tephra deposit with a sintered contact (c-d) Lava flow (HC1 and HC2) olivine displaying a reaction rim consisting of pigeonite (c), and lava flow (HC3) olivine surrounded by microcrystalline groundmass lacking a pigeonite reaction rim.
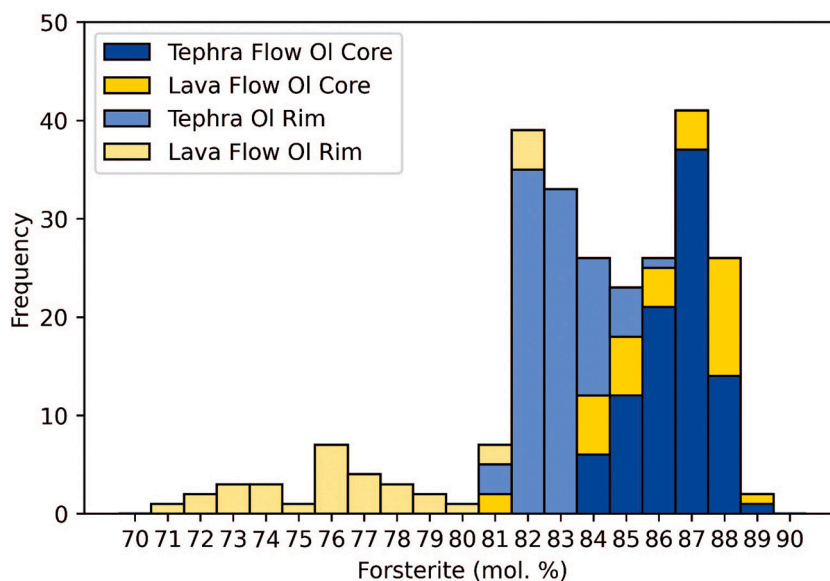

Fig. 5. Frequency histogram of olivine core and rim compositions from the tephra and lava.

4.3. Compositions of olivine-hosted melt inclusions and tephra glass

We analysed 30 melt inclusions within 25 tephra olivines. Corrected for PEC, MgO contents range from 7.8–11.5 wt% (Fig. 3a). In addition, we collected 74 analyses of the matrix glass surrounding the tephra olivines. The matrix glass displays a very narrow range in MgO from 6.6–7.0 wt% (Fig. 3a).

4.4. Mineralogy and textural observations

4.4.1. Tephra olivine

127 olivine crystals were picked from the reticulite clasts. These olivine crystals are mostly euhedral to subhedral and occur as both single crystals and in crystal clusters, sometimes with sintered contacts. The longest crystal dimension ranges from 300 μm to 3 mm (Fig. 4a and
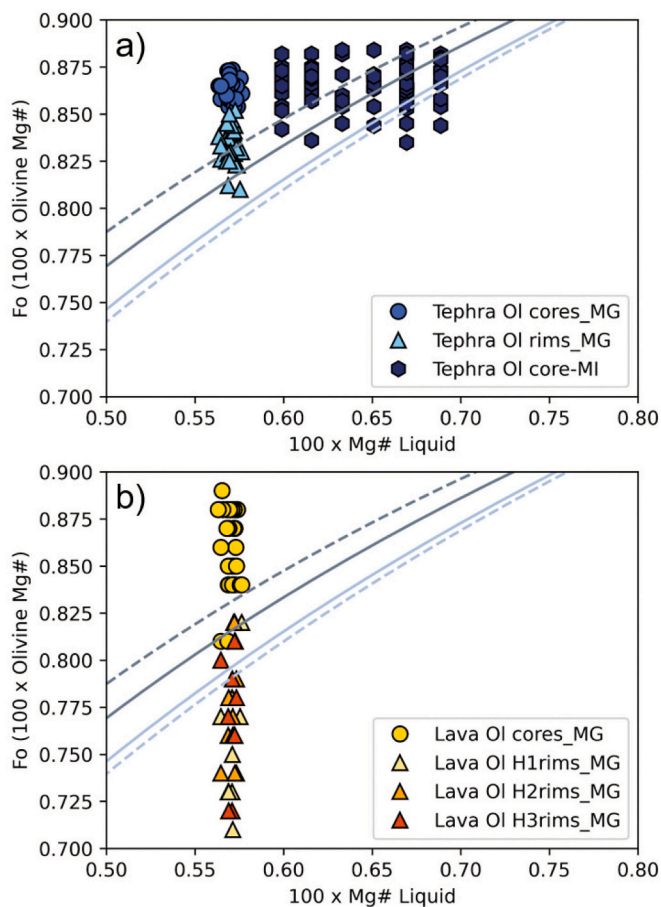
Fig. 6. *Rhodes diagram showing olivine-melt relationships for a) tephra and b) lava flow olivines.* (a) Core and rim olivine forsterite content versus tephra matrix glass (filled triangles and circles) and PEC-corrected melt inclusions (filled polygons). Mg-number (Mg#) for $Fe^{3+}/Fe_T = 0.15$ (Mousallam et al., 2016; Helz et al., 2017; Wieser et al., 2020). (b) Lava flow olivine core (filled circles) and rim compositions (by sample site, filled triangles). Olivine compositions plotting between the blue and the grey curve ($K_D = 0.27$–0.352) are in equilibrium with the carrier liquid considering a wide range of experimentally determined values for $K_{DFe^{2+}-Mg^{2+}}^{ol-melt}$ (blue curve: $K_D = 0.30 \pm 0.03$, Roeder and Emslie; Grey curve: $K_D = 0.34 \pm 0.012$, Matzen et al. (2011). (For interpretation of the references to colour in this figure legend, the reader is referred to the web version of this article.)

b). Zoned olivine crystals have Mg-rich cores and Fe-rich rims (normal zoning) with core compositions ranging from Fo_{89-84} (80% between Fo_{89-87}) and rim compositions ranging from Fo_{86-81} (Fig. 5). Zoned rims are ~40–80 μm wide. While most olivine crystals are zoned (70%), the unzoned olivines span a similar compositional range from Fo_{87-82}. The olivine crystals are host to an abundance of glassy melt inclusions that range in size from 10 μm to tens of μm in diameter (within a 2D section). These are found with and without oxide inclusions. Olivine crystals in clusters do not exhibit rims of more evolved Fo composition along the sintered contacts.

4.4.2. Lava flow olivine

Olivine crystals range in size from ~500 μm to 4 mm and have an estimated modal abundance of ~5–8% based on area fraction. 30% of olivines are euhedral, 70% are subhedral or rounded. Olivine crystals from H1 and H2 exhibit a reaction rim of variable thickness (~25–50 μm). This reaction rim is composed of pigeonite ((Mg/(Mg + Fe)x100) = 75–73, Ca/(Ca + Mg + Fe) = 0.08–0.1). (Fig. 4c). Olivines within H3 do not exhibit this corona (Fig. 4d). Olivine core values range from Fo_{89-81} but the majority of crystals (94%) are within the range Fo_{88-84}.

Rim compositions range more widely from Fo_{82-71} (Fig. 5). All olivines are normally-zoned (Mg-rich cores, Fe-rich rims), with typical rim widths of ~70–160 μm in samples H1CL and H2CL or ~ 40–60 μm in H3CL. Lava flow olivine crystals rarely contain melt inclusions, but where present they are fully crystallised. Some olivines contain inclusions of oxides up to 80 μm in length, often several crystals can be present per olivine.

4.5. Olivine-melt equilibria

Tephra glasses and PEC-corrected melt inclusion compositions were used to investigate olivine-melt relationships and to test whether the olivines were in equilibrium with their respective carrier melt at the time of the eruption. Olivine-melt equilibria were calculated between olivine core and tephra matrix glass, and olivine rims and tephra matrix glass for both tephra and lava flow olivine crystals (Fig. 6). We used an Fe3+ value of 0.15 (Mousallam et al., 2016; Helz et al., 2017; Wieser et al., 2021). We justify using the tephra matrix glass as a proxy for the lava flow groundmass, as the bulk rock data for the tephra and lava flow are similar, with the tephra composition closest to the most primitive lava composition. The upper bound of equilibrium is as defined by Matzen et al. (2011) ($Kd = 0.34 \pm 0.012$ (for $K_{DMg}^{2+} = (FeO/MgO)^{ol}/(FeO/MgO)^{liq}$)) and the lower bound of equilibrium is as defined by Roeder and Emslie (1970) ($Kd = 0.3 \pm 0.03$) to give the most appropriate error envelope.

Fig. 6 shows that tephra (Fig. 6a) and lava (Fig. 6b) olivine rims are generally found to be close to compositions predicted to be in equilibrium with the tephra matrix glass, with the exception of some more evolved lava olivine rims, which appear to have crystallised from melts more evolved than the tephra matrix glass. Tephra and lava olivine cores are too primitive to be in equilibrium with the matrix glass compositions. They appear, however, to be in equilibrium with a range of primitive melt inclusions compositions (Mg# 60–69).

4.6. Geothermometry

4.6.1. Olivine-melt thermometry

We applied mineral-melt thermometry to constrain the crystallisation temperature of the olivine cores. Olivine-melt temperatures have been calculated using eqs. 19 and 20 from Putirka (2008, standard error of estimate (SEE) of +/− 44 °C) based on the Beattie (1993) model. We use the PEC-corrected melt inclusion compositions ($n = 30$). Olivine-melt equilibrium pairs were selected following the criteria outlined in Putirka (2008), i.e. $K_D(Fe—Mg)^{ol-liq} = 0.30 \pm 0.03$ (1SEE) assuming anhydrous (< 1 wt% H_2O) conditions (Hauri, 2002). Olivine-melt inclusion temperatures range from 1210 °C to 1293 °C with a mean value of 1260 °C (±44 °C). Over 90% of the melt inclusions were located within the homogenous part of the olivines towards the cores.

4.6.2. Melt-only thermometry

The matrix glass, in contact with the rims of the olivines, was quenched rapidly upon eruption. Thermometry calculations ($n = 74$) using the Helz and Thornber (1987) liquid-only thermometer, provide lower temperatures within the range 1147–1154 °C with a mean of 1151 °C $\pm$ 10 °C (1σ). Kernel density estimates for all calculated temperatures can be found in the Supplementary Materials. As the diffusion zone occurs around the edge of the olivines in contact with the matrix glass, we use this calculated temperature as an input parameter for our diffusion models.

4.7. Fe—Mg interdiffusion chronometry

Diffusion timescales were calculated using AUTODIFF, a 1D finite difference algorithm as described in Hartley et al. (2016), Pankhurst et al. (2018) and Couperthwaite et al. (2020, 2021). A demonstration version of this model can be found in the Supplementary Data. We
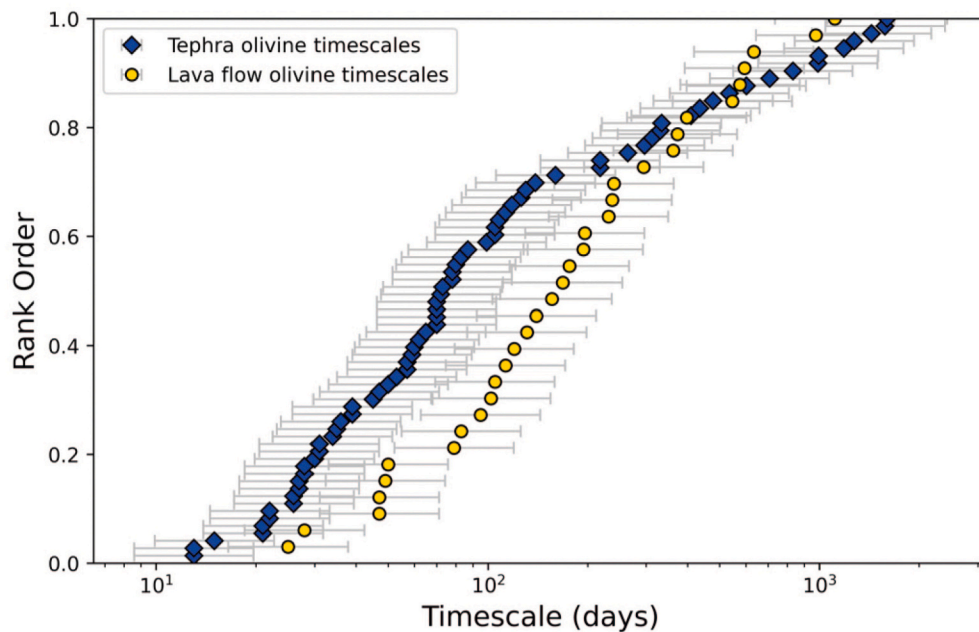
Fig. 7. *Rank order plot displaying Fe—Mg interdiffusion timescale distributions for tephra (blue diamonds) and lava flow (yellow circles) olivines. Time in logarithmic scale. Error bars represent an average uncertainty on each timescale of ±0.18 log units. Both distributions show a high frequency of shorter timescales (<100 days) and a lower frequency of longer timescales (>200 days). (For interpretation of the references to colour in this figure legend, the reader is referred to the web version of this article.)*

applied a homogenous initial condition and a fixed externally-buffered boundary condition (effectively Dirichlet-type conditions) to each diffusion profile extracted from the tephra and lava flow olivines. The methodology for calibrating BSE/EMP profiles for input into the diffusion model is described in (Couperthwaite et al., 2020)

The same modelling parameters of T, P and fO_2 were used for both the tephra olivines and lava flow olivines. The tephra matrix glass thermometry was used as a proxy for the lava flow ground mass due to the similarity in bulk rock compositions between the tephra and lava flow. Timescales were calculated using a temperature of 1151 °C and a maximum pressure of 0.2 GPa. The oxygen fugacity was set at the QFM buffer (Gerlach, 1993). Diffusion down the c-axis of olivine is ~6 times faster than along the a- or b-axis (Costa and Chakraborty, 2004; Dohmen et al., 2007; Dohmen and Chakraborty, 2007a, 2007b) hence all timescales were corrected for anisotropy. No corrections for shallow sectioning angle have been applied to the modelled timescales. According to Couperthwaite et al. (2021), for larger crystals (up to 2–3 mm) with a narrow diffusion width relative to their size, sectioning effects will be negligible on the calculated timescales. For the smaller crystals (less than 1 mm), any overestimate due to shallow sectioning effects are likely to be within error on the timescale uncertainty for most datasets. Fig. 7 shows the range and frequency of modelled timescales for olivine from both the tephra and lava samples.

We modelled 73 timescales from 34 tephra olivine crystals. The absolute calculated timescales for tephra olivines range from 13 to 1600 days with an average uncertainty on each calculated timescale of 0.18 log units (1σ). The uncertainty is calculated using Monte Carlo calculations incorporating the uncertainty for temperature, the pre-exponential factor (D_0), activation energy, oxygen fugacity, pixel size, profile width and noise within the SEM image. Uncertainties on pre-exponential factor and activation energy are treated as co-varying due to their methods of determination (Dohmen and Chakraborty, 2007a, 2007b). Table 3 shows all modelled timescales and their absolute uncertainties. We calculate that ~70% (51) of the timescales are less than 100 days (~3 months).

Thirty-eight compositional profiles were retrieved from 14 olivine crystals (6 from H1LC, 4 from H2CL, and 4 from H3CL) within the lava flow samples. Absolute timescales from lava flow olivines range from 25 to 1110 days with an average uncertainty on each calculated timescale of 0.18 log units (1σ). We calculate that ~30% (9) of the timescales are

less than 100 days (~3 months).

5. Discussion

5.1. Comparison of tephra and lava flow olivines

5.1.1. Composition and timescale contrasts

The lack of variation within the whole rock major element compositions indicate that the tephra and lava flow represent similar magma compositions and likely contain the same proportion of crystalline olivine.

The lava and tephra olivine crystals have almost identical core compositions within the range Fo$_{89-84}$. Rim compositions of flow olivines, at Fo$_{83-71}$, are notably more evolved than the rims of Fo$_{86-81}$ found in the tephra. This is interpreted as a consequence of continued rim growth (and diffusion) of the olivines during protracted cooling in the lava flow compared to rapid quenching of the tephra. The shortest absolute diffusion timescale for lava flow olivine is 25 days compared to 13 days for tephra olivine. Although these timescales overlap when accounting for uncertainties, tephra olivines record on average shorter timescales with two thirds of timescales being less than 100 days.

5.1.2. Pigeonite overgrowths

Aside from a difference in rim compositions and diffusion timescales, the other striking difference between the tephra and lava flow olivines is the presence of a pigeonite rim surrounding all lava flow olivines contained in samples H1 and H2. The lack of pigeonite rims in tephra olivines is again likely due to the rapid quenching of the tephra upon eruption. The pigeonite rim is further evidence that some of the olivine crystals are out of chemical equilibrium with their host liquid. This could be due to co-growth of pigeonite and olivine along the cotectic whilst in the lava flow (before cooling), evidenced by partial inclusion of the pigeonite crystals within the olivine as shown in Fig. 8. Or, it could reflect a disequilibrium reaction between olivine and a more silica-rich magma due to mixing (Gerlach and Grove, 1982; Coombs and Gardner, 2004; Erdmann et al., 2012). The lack of pigeonite rims around H3 olivines maybe be due to a higher degree of cooling positioned at the top of the lava flow field or residence in a more homogenous magma composition.

The pigeonites cross-cut the diffusion front (Fig. 8), an important

Table 3
Calculated timescales (days) for Fe—Mg diffusion in olivine.

Sample type	Profile	Timescale (days)	t (+)	t (−)
Tephra	Block 2_C2	13	7	4
Tephra	Block 5_G1	13	7	4
Tephra	Block 4_C2_4	15	8	5
Tephra	Block 5_G2ii_2	21	11	7
Tephra	Block 4_K2	21	11	7
Tephra	Block 4_Q3	22	11	7
Tephra	Block 5_E2	22	11	7
Tephra	Block 4_A1	26	13	9
Tephra	Block 5_G2	26	13	9
Tephra	Block 4_K1	27	14	9
Tephra	Block 3_H3	27	14	9
Tephra	Block 4_C2_3	28	14	10
Tephra	Block 5_O2	28	14	10
Tephra	Block 4_Q1	30	15	10
Tephra	Block 2_F3	31	16	11
Tephra	Block 5_G2ii_1	31	16	11
Tephra	Block 4_C2_1	34	17	12
Tephra	Block 4_Q4	35	18	12
Tephra	Block 5_E1	36	18	12
Tephra	Block 2_F2	39	20	13
Tephra	Block 4_O1	39	20	13
Tephra	Block 5_C2	45	23	15
Tephra	Block 2_F1	47	24	16
Tephra	Block 4_E1	50	26	17
Tephra	Block 4_C2_2	53	27	18
Tephra	Block 5_C4	57	29	19
Tephra	Block 5_G2ii_3	57	29	19
Tephra	Block 2_A1	59	30	20
Tephra	Block 2_J1	60	31	20
Tephra	Block 3_G part2_2	62	32	21
Tephra	Block 2_G2	65	33	22
Tephra	Block 4_E3	70	36	24
Tephra	Block 2_B2	70	36	24
Tephra	Block 2_G1	70	36	24
Tephra	Block 2_C1	70	36	24
Tephra	Block 5_O1	72	37	24
Tephra	Block 3_K2	73	37	25
Tephra	Block 4_Q2	78	40	26
Tephra	Block 4_E2	78	40	26
Tephra	Block 3_K1	80	41	27
Tephra	Block 3_N2	83	43	28
Tephra	Block 2_J2	87	45	30
Tephra	Block 2_B1	99	51	34
Tephra	Block 5_O3	105	54	36
Tephra	Block 5_C1	105	54	36
Tephra	Block 3_K3	108	55	37
Tephra	Block 4_D1	113	58	38
Tephra	Block 5_C3	118	61	40
Tephra	Block 2_C3	126	65	43
Tephra	Block 4_D3	130	67	44
Tephra	Block 4_E2_2	139	71	47
Tephra	Block 2_G3	160	82	54
Tephra	Block 5_K3	218	112	74
Tephra	Block 5_H2	218	112	74
Tephra	Block 4_E2_1	264	136	90
Tephra	Block 5_K2	297	153	101
Tephra	Block 4_I_2	313	161	106
Tephra	Block 5_H3	331	170	112
Tephra	Block 4_I_1	334	172	113
Tephra	Block 2_I3	410	211	139
Tephra	Block 2_N1	436	224	148
Tephra	Block 2_I2	478	245	162
Tephra	Block 2_D2	535	275	182
Tephra	Block 3_W3	602	309	204
Tephra	Block 2_N2	708	364	240
Tephra	Block 2_N4	832	427	282
Tephra	Block 3_C3	990	508	336
Tephra	Block 3_W2	995	511	338
Tephra	Block 3_W1	1185	609	402
Tephra	Block 3_C1	1274	654	432
Tephra	Block 2_I1	1437	738	488
Tephra	Block 3_C2	1577	810	535
Tephra	Block 2_D4	1600	822	543
Lava flow	H3CL_C4	25	13	8

Table 3 (*continued*)

Sample type	Profile	Timescale (days)	t (+)	t (−)
Lava flow	H3CL_C3	28	14	10
Lava flow	H3CL_C5	47	24	16
Lava flow	H3CL_C2	47	24	16
Lava flow	H3CL_B1	49	25	17
Lava flow	H3CL_D1	50	26	17
Lava flow	H3CL_D2	79	41	27
Lava flow	H3CL_C1	83	43	28
Lava flow	H1LC_A2	95	49	32
Lava flow	H1LC_B3	102	52	35
Lava flow	H1LC_B2	105	54	36
Lava flow	H3CL_A1	113	58	38
Lava flow	H1LC_B1	120	62	41
Lava flow	H2CL_B1	131	67	44
Lava flow	H1LC_C1	140	72	48
Lava flow	H1LC_E2	156	80	53
Lava flow	H1LC_C3	168	86	57
Lava flow	H1LC_A3	176	90	60
Lava flow	H1LC_C2	194	100	66
Lava flow	H2CL_B2	196	101	67
Lava flow	H1LC_D2	231	119	78
Lava flow	H1LC_F1	237	122	80
Lava flow	H1LC_D1	240	123	81
Lava flow	H1LC_D3	295	152	100
Lava flow	H2CL_B4	362	186	123
Lava flow	H2CL_D1	373	192	127
Lava flow	H3CL_A2	398	204	135
Lava flow	H2CL_C3	546	280	185
Lava flow	H1LC_E1	576	296	195
Lava flow	H2LC_A1	594	305	202
Lava flow	H2CL_C1	634	326	215
Lava flow	H2LC_A2	975	501	331
Lava flow	H2CL_D2	1112	571	377

textural indicator suggesting either that;

1. The onset of diffusion within the lava flow olivines started prior to pigeonite rim overgrowth, but also that the pigeonite rim has formed by reaction with the exterior of the olivine
2. There has been some overgrowth on the olivine during the diffusion process and synchronous with the pigeonite formation, to embed them into the rim.

The suggestion that there has been olivine overgrowth is consistent with the observation that the rim composition in the lava samples extend to lower forsterite values than those found in the tephras, which suggest the equilibria were tracking to lower temperatures and would be consistent with olivine growth during diffusion (Couperthwaite et al., 2021). Consequently, interpretation of the lava flow olivine diffusion timescales is complicated by their post-eruptive history. If the pigeonite rim has digested some diffusion zoning that would make them *minimum* timescales, as we do not know how much of the olivine rims were lost due to late-stage pigeonite overgrowth. If the crystals have had extra olivine rim growth in the lava flow during diffusion that would conversely cause an *overestimation* of timescales. In addition, they likely formed during protracted cooling, so the diffusion process would have not been isothermal, inducing more uncertainty and scatter into the results.

5.2. Determining the meaning of the olivine timescales

In interpreting the diffusion chronometry data, it becomes key to try to understand what the timescales actually represent. Textural clues suggest that the chronometry data represent the equilibration timescales between incorporated crystals and a new carrier melt. This is evidenced by the abundance of crystal clots and micro-xenoliths of olivine-rich material where external faces have developed diffusive rims whilst the interiors have not (Supplementary Materials). Further evidence is the apparent disequilibrium between the primitive olivine cores and the
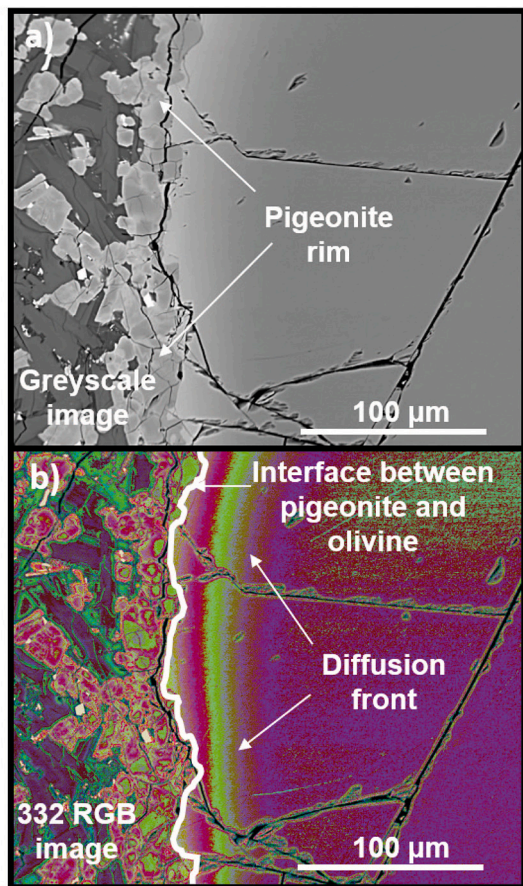
Fig. 8. *(a) Greyscale BSE image and (b) false colour (332RGB) BSE image of pigeonite rim on a lava flow olivine from H1CL.* The pigeonite rim clearly cross cuts the diffusion front (highlighted by the white line contour line).

carrier melt (Fig. 6). The diversity of timescales therefore represents an ongoing process of crystal mush incorporation into a new host liquid/melt. This is analogous to mechanisms proposed for other hotspot volcanoes (e.g. Piton de la Fournaise (Albert et al., 2019), El Hierro, Canary Islands (Longpré et al., 2014) and several volcanoes in Iceland (Caracciolo et al., 2021).

5.3. Olivine crystal histories, mush disruption and magma mobilisation

Given the above complexities in interpreting the lava flow samples, any discussion of the pre-eruptive magmatic history is best defined through the olivine populations of the tephra. Fig. 9a and b shows a compilation of all olivine forsterite profiles extracted from tephra and lava flow olivines. Tephra olivines display profile shapes with variable zoning widths allowing two different types (I and II) to be identified: Type I, comprising 70% of the population are profiles with typically narrow zoning widths of ~40 um and rim compositions within the range Fo_{86-81}. Type II, making up the remaining 30% of the population are profiles characterized by broader zoning widths (~80 um) and more restricted rim compositions (of Fo_{83-81}). Fig. 9c and d shows best fit diffusion models for type I and type II tephra olivines. In terms of diffusion timescales, the majority (87%) of type I tephra olivines record timescales of 100 days or less, whereas the bulk of type II olivines register timescales of 250 days and longer (Fig. 10).

Lava flow olivines from sample H3CL record shorter timescales (up to ~79 days; 75%) than olivines from samples H1Cl and H2CL (95–1110 days; 100%). We suggest that this is due to the stratigraphic position of lobe H3 (above H1 and H2) enabling it to cool faster (evidenced by the lack of pigeonite rims and finer groundmass) and

providing greater insulation for continued diffusive relaxation within lobes H1 and H2. The earliest diffusion timescales that are offset to the main trend on Fig. 10, are from H3 olivines. The longer H1 and H2 timescales occur despite the observed pigeonite overgrowth rims on H1CL and H2 CL olivines.

At Kīlauea, Wieser et al. (2019) state that olivine mush piles are widely acknowledged to be located in close proximity to magma storage reservoirs as indicated by regions of high seismic velocity. At Mauna Loa, high velocity regions (6.5–7.5 km/s) occur from 0 to 10 km depth beneath the summit, but also exist below the lower SWRZ from 0 to 6 km depth; they are interpreted to be mafic cumulates (Okubo et al., 1997; Park et al., 2007; Lin et al., 2014).

We suggest that high MgO melts represented by the most primitive melt inclusions (7.8 to 11.5 MgO wt%%) may have crystallised the majority of olivine core compositions within a cumulate zone at some depth beneath the rift. This is comparable to the ideas around olivine mush storage advanced by Thomson and Maclennan (2013) who also suggest that olivines may undergo significant diffusive re-equilibration during mush storage, reducing the variability of olivine compositions expressed as XFo. In the case of Hapaimamo, some variability in Fo in the cores appears to have been retained. Similar variability is also found within Kīlauea olivine cores (Lynn et al., 2017). In terms of how the Hapaimamo system evolved, mush disruption by an intruding melt occurred over months to years before eruption, indicated by the range of diffusion timescales. This process was gradual, with crystals developing more evolved rims and diffusing over time, and new diffusion chronometers starting as mush clusters disaggregated by convection and abrasion and new olivine surfaces were exposed to the melt. Rims of type II (broader profiles) olivines record a more restricted compositional range (Fo_{83-81}) indicating that earlier intruded magma may be well-mixed, whereas later intruding magma causing the formation of type I (narrower profiles) olivines was less well mixed as evidenced by more variable rim compositions. Alternatively, these more variable rim compositions could also reflect time spent in different compositional and thermal environments.

The increase in frequency of shorter timescales closer to eruption may reflect a more efficient mush disaggregation mechanism. As well as efficiency, the type I and type II profiles may reflect the granular dynamics of mush mobilisation. Models by Cheng et al. (2020) suggest that with increasing residence time the proportion of zoned crystals mobilised increases, together with the length scale of crystal zoning (Type II). In addition, the variability of rim compositions initially increases then decreases (Type I → Type II). As the youngest diffusion timescales are 13 days (9 days when accounting for the uncertainties), mush disaggregation activity probably stopped in the week prior to eruption.

5.4. Comparing olivine diffusion timescales from Mauna Loa and Kīlauea

This study and Couperthwaite et al. (2020), provide the first records of Fe—Mg interdiffusion timescales for Mauna Loa eruption products. By contrast, neighbouring Kīlauea Volcano has been the subject of multiple diffusion studies covering recent (1959 CE Kīlauea Iki eruption; Rae et al., 2016; Bradshaw et al., 2018) and prehistoric (1500–1820 A. D. Keanakākoʻi tephra eruption; Lynn et al., 2017) events (Fig. 11). A comparison of these results across the two volcanic systems may therefore be in order, to see if any broader inferences can be made. It is however important to note that each Kīlauea eruption summarised below occurred near to the summit region, in contrast to the Hapaimamo eruption, that occurred down rift, within the SWRZ of Mauna Loa.

Couperthwaite et al. (2020) suggest timescales of months to years for accumulation of polyhedral olivine from a deep source and subsequent transport to shallow storage where they remained prior to the prehistoric Moinui eruption 2000 years B.P. All olivines were normally zoned and their maximum timescales and the range of timescales are similar to those calculated for olivines of the Hapaimamo eruption, suggesting similar magmatic processes for both eruptions. Lynn et al.
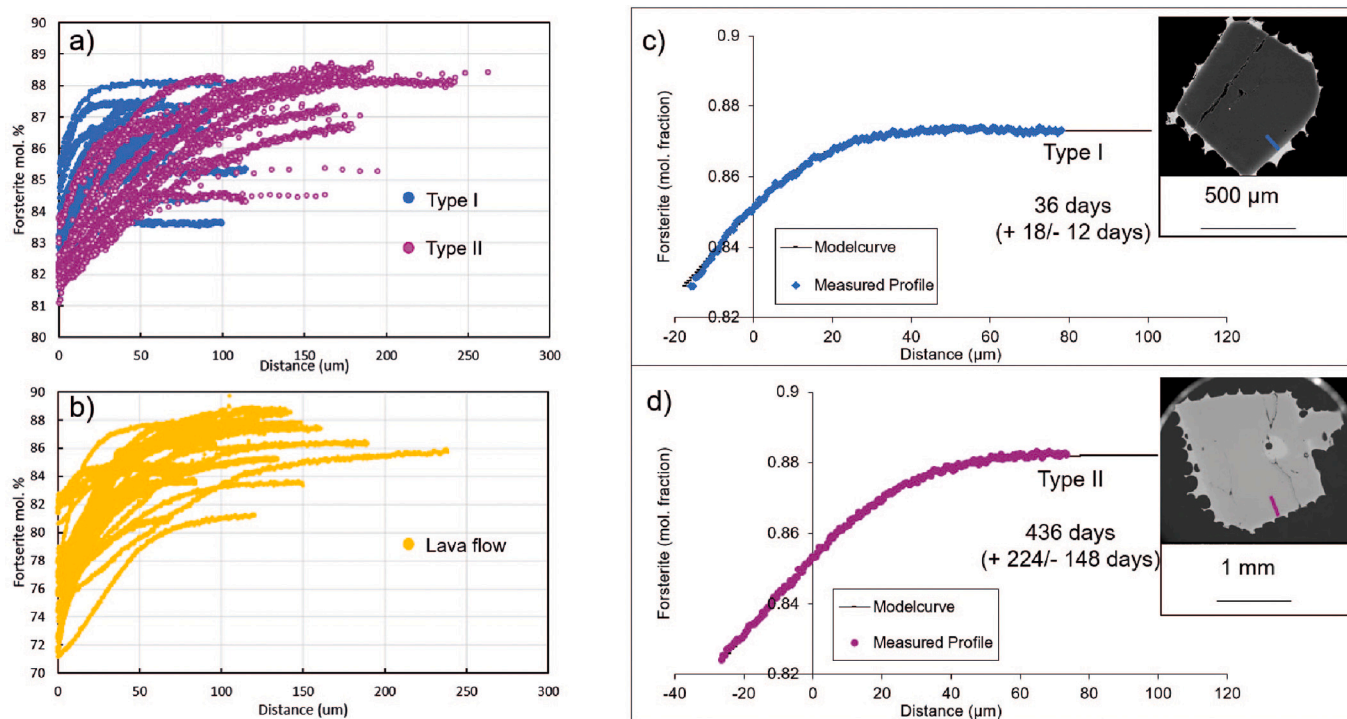
Fig. 9. *Fe—Mg interdiffusion profile shapes.* Combined olivine zoning record showing a compilation of core-to-rim forsterite profiles from (a) tephra and (b) lava flow olivines. Tephra olivines display type I and type II profile shapes with variable zoning widths and rim compositions. (c-d) Examples of best fit diffusion models for type I and type II tephra olivines including modelling timescales and 1σ uncertainties. Coloured lines in BSE images show directions of analytical traverses.
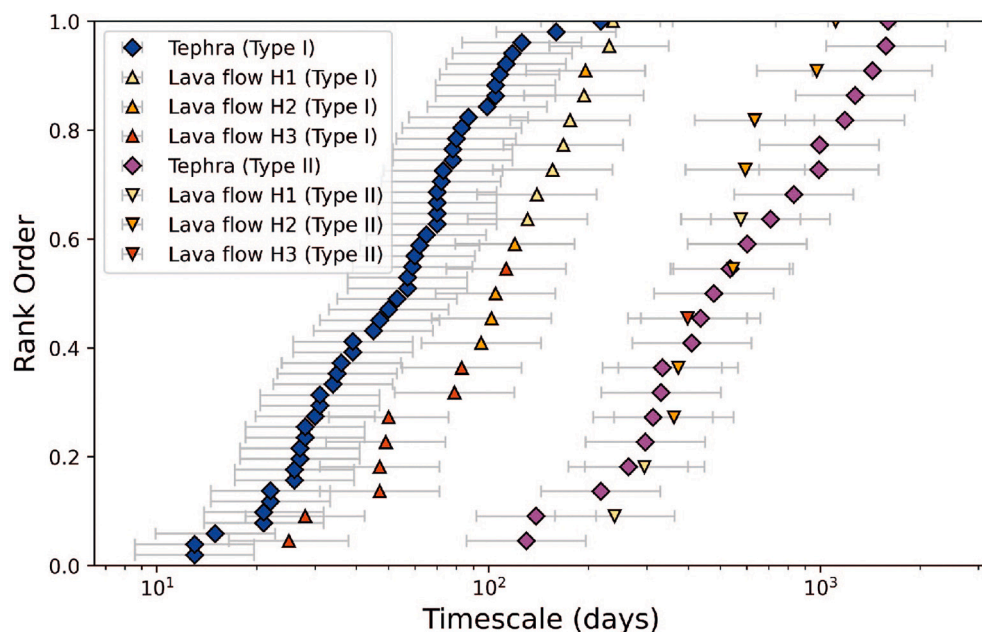

Fig. 10. *Cumulative density function (CDF) of Fe—Mg interdiffusion timescales for different olivine types from tephra and lava flow samples.* Blue diamonds show that 87% of type I tephra olivine timescales are less than 100 days. Magenta diamonds show 87% of type II tephra olivine timescales are more than 250 days. Filled triangles shows lava olivine timescales by samples site and type with similar distribution to the tephra olivines. Absolute timescales trend longer than timescales from tephra olivines. (For interpretation of the references to colour in this figure legend, the reader is referred to the web version of this article.)

(2017) observed normal, reverse, and complex zoning within olivines of the historical Keanakāko'i tephra eruption. Related Fe—Mg interdiffusion and Ni diffusion timescales are on the order of weeks to several years for pre-eruptive magma mixing and storage. Diffusion timescales obtained for the outermost rims of complexly zoned olivines are short on the order of hours to days suggesting an additional late-stage mixing event shortly prior to eruption. No reverse or complex zoning has been identified in olivines from Mauna Loa within the Moinui or Hapaimamo eruptions. However, Couperthwaite et al. (2020) showed that evolved

olivine cores in the Moinui samples, nucleated and grew into platy morphologies and subsequently diffused shortly before eruption.

More recent Kīlauea eruptions, such as the 1959 CE Kīlauea Iki Crater event, also contain evidence for multi-level open-system magma mixing processes in the form of diverse olivine zoning records ranging from normal to reverse and complex, with normal being the most dominant (Rae et al., 2016). Olivine Fe—Mg interdiffusion chronometry suggests a sequence of mixing events, with the first event having occurred as far back as 2 years prior to eruption in the deep storage
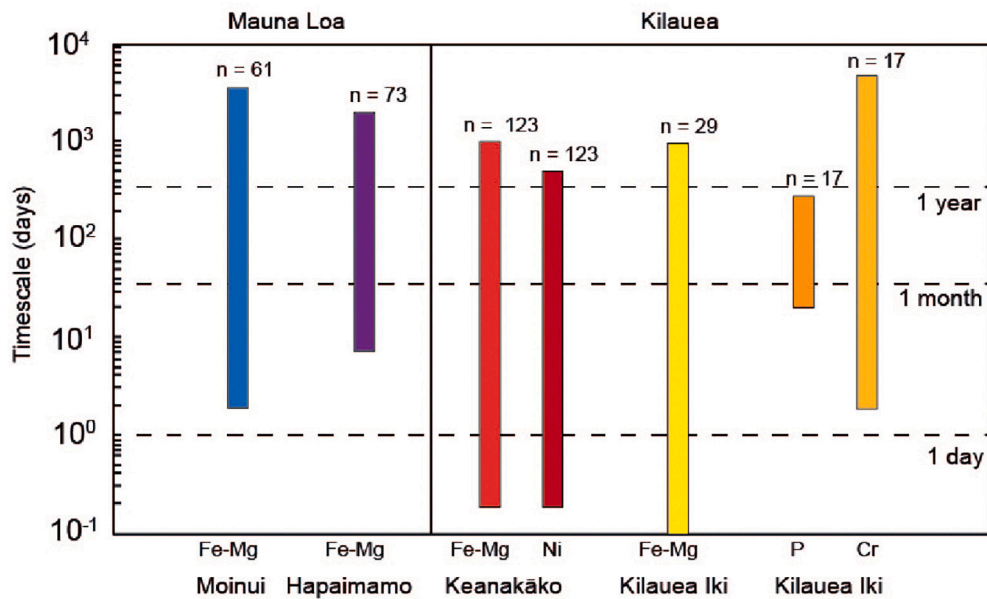
Fig. 11. *Compilation of olivine diffusion timescales for Mauna Loa and* Kīlauea. Each colour bar represents the full range of observed timescales from each study. Note that the timescale is logarithmic. From left to right: Moinui lava flow, Mauna Loa (Couperthwaite et al., 2020); Hapaimamo tephra, Mauna Loa (this study); Keanakāko'i tephra, Kīlauea (Lynn et al., 2017); Kīlauea Iki tephra (Rae et al., 2016); Kīlauea Iki tephra (Bradshaw et al., 2018).

system. A second, shallower mixing event occurred in the weeks and months prior to the eruption between intruding hot melt and more evolved resident liquids. The final mixing event occurred in the hours and days before eruption in the shallow reservoir and conduit. Bradshaw et al. (2018) used diffusion chronometry of phosphorous (P) and chromium (Cr) in olivine picrites from the Kīlauea Iki eruption to constrain magma residence times. Based on the P and Cr diffusion modelling results, two distinct olivine populations were identified recording different magma residence times ranging between 10 days to 43 years (population I) and 2 days and 4 months (population II).

Each of these studies (including this one) report comparable forsterite core compositions of $\sim Fo_{89-82}$, suggesting Kīlauea and Mauna Loa olivines could be derived from similar parts of the plumbing system. Both Lynn et al. (2017) and Couperthwaite et al. (2020) suggest olivines with higher forsterite core compositions ($\sim Fo_{89-85}$) originate from deeper, more primitive magmas whereas those with more evolved core compositions ($\sim Fo_{84-80}$) formed at shallower crustal levels, and therefore related diffusion timescales are more indicative of magmatic processes occurring in the shallower part of the plumbing system. We note, however, that no such distinctions were made by Rae et al. (2016) and Bradshaw et al. (2018) with regards to forsterite content.

Calculated diffusion timescales for Moinui or Hapaimamo olivines span a similar range of timescales to those calculated for Kīlauea. Although this study lacks olivine trace element data for direct comparison, magma mobilisation and transfer processes within both magmatic systems appear to occur over similar timescales (Figure 11). Both systems also show evidence of rapid late-stage processes occurring in the days before eruption (e.g., core nucleation or rim growth) against a background of more protracted magma processes dating back months to years. Further studies are needed across a more representative suite of Mauna Loa deposits for more direct comparisons of pre-eruptive magmatic processes.

6. Conclusions

We have presented a petrological and diffusion chronometry study of conditions and dynamics of mush disaggregation recorded in the products of the pre-historic ($\sim$240 B. P.) Hapaimamo eruption of Mauna Loa.

Olivine crystals from tephra of the 'Akau unit of the Hapaimamo

eruption at Mauna Loa give the most robust data towards understanding pre-eruptive magmatic processes. Olivine diffusion timescales are linked to crystal mobilisation from a disaggregating mush beneath the rift zone, which commences up to years prior to eruption. Tephra olivine falls into two main categories (type I and type II) defined by diffusion width and olivine rim compositions, suggesting either two episodes or two processes separate in time and potentially space in the months prior to eruption or a change in rate in processes $\sim$200 days prior to eruption. Although tephra and lava flow timescales overlap when accounting for uncertainties, tephra olivines record on average shorter timescales with two thirds of timescales being less than 100 days. Tephra olivines are also not susceptible to overgrowth and cooling temperatures whilst diffusion is ongoing, as in the lava flow. Comparison of elemental diffusion timescales from Mauna Loa with those from Kīlauea shows that magma mobilisation and transfer processes seem to occur over similar timescales.

CRediT authorship contribution statement

F.K. Couperthwaite: Conceptualization, Data curation, Formal analysis, Methodology, Project administration, Visualization, Writing - original draft. **D.J. Morgan:** Conceptualization, Funding acquisition, Methodology, Software, Supervision, Investigation, Resources, Validation, Writing - review & editing. **J. Harvey:** Formal analysis, Investigation, Supervision, Resources, Validation, Writing - review & editing. **M. Kahl:** Formal analysis, Investigation, Supervision, Validation, Writing - review & editing.

Declaration of Competing Interest

The authors declare that they have no known competing financial interests or personal relationships that could have appeared to influence the work reported in this paper.

Data availability

Data and modelling code used is included in the Supplementary Materials

Acknowledgements

We would like to thank Frank Trusdell for aiding with field access and sample collection. We would also like to thank Luke Wedmore for his help in the field. John Wynn Williams and Richard Walshaw are thanked for their assistance with sample preparation and the analytical facilities at the University of Leeds.

Appendix A. Supplementary data

Supplementary data to this article can be found online at https://doi.org/10.1016/j.jvolgeores.2022.107690.

References

Albert, H., Costa, F., Di Muro, A., Herrin, J., Metrich, N., Deloule, E., 2019. Magma interactions, crystal mush formation, timescales, and unrest during caldera collapse and lateral eruption at ocean island basaltic volcanoes (Piton de la Fournaise, La Reunion). Earth Planet. Sci. Lett. 515 (1), 187–199.

Barnard, W.M., 1995. Mauna Loa Volcano: Historical eruptions, exploration, and observations (1779–1910). In: Mauna Loa Revealed: Structure, Composition, History and Hazards, Geo, pp. 1–19.

Beattie, P., 1993. Olivine-melt and orthopyroxene-melt equilibria. Contributions to Mineralogy and Petrology 115, 253–270.

Bradshaw, R.W., Kent, A.J.R., Tepley, F.J., 2018. Chemical fingerprints and residence times of olivine in the 1959 Kilauea Iki eruption, Hawaii: Insights into picrite formation. Am. Mineral. 103 (11), 1812–1826.

Caracciolo, A., Kahl, M., Bali, E., Guðfinnsson, G.H., Halldórsson, Hartley, M.E., 2021. Timescales of crystal mush mobilization in the Bárðarbunga-Veiðivötn volcanic system based on olivine diffusion chronometry. Am. Mineral. 106 (7), 1083–1096.

Cheng, L., Costa, F., Bergantz, G., et al., 2020. Linking fluid dynamics and olivine crystal scale zoning during simulated magma intrusion. Contributions to Mineralogy and Petrology 175 (6).

Coombs, M.L., Gardner, J.E., 2004. Reaction rim growth on olivine in silicic melts: Implications for magma mixing. Am. Mineral. 89 (5–6), 748–759.

Costa, F., Chakraborty, S., 2004. Decadal time gaps between mafic intrusion and silicic eruption obtained from chemical zoning patterns in olivine. Earth Planet. Sci. Lett. 227 (3–4), 517–530.

Costa, F., Chakraborty, S., Dohmen, R., 2003. Diffusion coupling between trace and major elements and a model for calculation of magma residence times using plagioclase. Geochim. Cosmochim. Acta 67 (12), 2189–2200.

Couperthwaite, F.K., Thordarson, T., Morgan, D.J., Harvey, J., Wilson, M., 2020. Diffusion timescales of magmatic processes in the Moinui lava eruption at Mauna Loa, Hawai'i, as inferred by bimodal olivine populations. J. Petrol. 61.

Couperthwaite, F.K., Morgan, D.J., Pankhurst, M.J., Lee, P.D., Day, J.M.D., 2021. Reducing epistemic and model uncertainty in ionic inter-diffusion chronology: a 3D observation and dynamic modeling approach using olivine from Piton de la Fournaise, La Reunion. American Mineralogist 106 (3).

Danyuchevsky, L.V., Della-Pasqua, F.N., Sokolov, S., 2000. Re-equilibration of melt inclusions trapped by magnesian olivine phenocrysts from subduction-related magmas: petrological implications. Contrib. Mineral. Petrol. 138 (1), 68–83.

Danyuschevsky, L.V., Plechov, P., 2011. Petrolog3: Integrated software for modeling crystallization processes. Geochem. Geophys. Geosyst. 12 (7).

Decker, R.W., Koyanagi, R.Y., Dvorak, J.J., Lockwood, J.P., Okamura, A.T., Yamashita, K.M., Tanigawa, W.R., 1983. Seismicity and Surface Deformation of Mauna Loa Volcano, Hawaii. Eos 64, 545–547.

Dohmen, R., Chakraborty, S., 2007a. Fe–Mg diffusion in olivine II: point defect chemistry, change of diffusion mechanisms and a model for calculation of diffusion coefficients in natural olivine. Phys. Chem. Miner. 34 (6), 409–430.

Dohmen, R., Chakraborty, S., 2007b. Erratum: Fe–Mg diffusion in olivine II: point defect chemistry, change of diffusion mechanisms and a model for calculation of diffusion coefficients in natural olivine. Phys. Chem. Miner. 34 (6), 409–430.

Dohmen, R., Becker, H.-W., Chakraborty, S., 2007. Fe–Mg diffusion in olivine I: experimental determination between 700 and 1,200°C as a function of composition, crystal orientation and oxygen fugacity. Phys. Chem. Miner. 34 (6), 389–407.

Erdmann, S., Scaillet, B., Kellett, D.A., 2012. Textures of Peritectic Crystals as Guides to Reactive Minerals in Magmatic Systems: New Insights from Melting experiments. J. Petrol. 53 (11), 2231–2258.

Fitton, J.G., Goddard, M., 2004. Origin and evolution of magmas on the Ontong Java Plateau. Geological Society of London Special Publications 229, 151–178.

Fitton, J.G., Saunders, A.D., Larsen, L.M., Hardarson, B.S., Norry, M.J., 1998. Volcanic rocks from the Southeast Greenland margin at 63° N: Composition, petrogenesis and mantle sources. Proc. Ocean Drill. Program Sci. Results 152, 331–350.

Gaffney, A.M., 2002. Environments of Crystallization and Compositional Diversity of Mauna Loa Xenoliths. J. Petrol. 43 (6), 963–981.

Garcia, M., Rhodes, M., 2012. AGU Chapman Conference Fieldtrip Guide, South West Mauna Loa.

Garcia, M.O., Hulsebosch, T.P., Rhodes, J.M., 1995. Olivine rich submarine basalts from the southwest rift zone of Mauna Loa Volcano: Implications for magmatic processes and geochemical evolution. In: Mauna Loa Revealed: Structure, Composition, History, and Hazards. Geophysical Monograph, 92.

Gerlach, T.M., 1993. Oxygen buffering of Kilauea volcanic gases and the oxygen fugacity of Kilauea basalt. Geochim. Cosmochim. Acta 7 (4), 795–814.

Gerlach, D.C., Grove, T.L., 1982. Petrology of Medicine Lake Highland volcanics: Characterization of endmembers of magma mixing. Contrib. Mineral. Petrol. 80 (2), 147–159.

Hartley, M.E., Thordarson, T., 2013. The 1874-1876 volcano-tectonic episode at Askja, North Iceland: Lateral flow revisited. Geochem. Geophys. Geosyst. 14 (7), 2286–2309.

Hartley, M.E., Morgan, D.J., Maclennan, J., Edmonds, M., Thordarson, T., 2016. Tracking timescales of short-term precursors to large basaltic fissure eruptions through Fe–Mg diffusion in olivine. Earth and Planetary Science Letters 439, 58–70. Elsevier B.V.

Harvey, J., Yoshikawa, M., Hammond, S.J., Burton, K.W., 2012. Deciphering the trace element characteristics in Kilbourne hole peridotite xenoliths: Melt-rock interaction and metasomatism beneath the Rio Grande Rift, SW USA. J. Petrol. 53 (8), 1709–1742.

Hauri, E., 2002. SIMS analysis of volatiles in silicate glasses, 2: isotopes and abundances in hawaiian melt inclusions. Chem. Geol. 183, 115–141.

Helz, R.T., Thornber, C.R., 1987. Geothermometry of Kilauea Iki lava lake. Hawaii. Bulleting of Volcanology 49, 651–668.

Helz, R., Cottrell, E., Brounce, M.N., Kelley, K.A., 2017. Olivine-melt relationships and syneruptive redox variations in the 1959 eruption of Kilauea volcano as revealed by XANES. J. Volcanol. Geotherm. Res. 333, 1–14.

Humphreys, M.C.S., Menand, T., Blundy, J.D., Klimm, K., 2008. Magma ascent rates in explosive eruptions: Constraints from H$_2$O diffusion in melt inclusions. Earth Planet. Sci. Lett. 270 (1–2), 25–40.

Jarosewich, E., Nelen, J.A., Norberg, J.A., 1980. Reference samples for electron microprobe analysis. Geostand. Geoanal. Res. 4 (1), 43–47.

Kahl, M., Chakraborty, S., Costa, F., Pompilio, M., 2011. Dynamic plumbing system beneath volcanoes revealed by kinetic modeling, and the connection to monitoring data: an example from Mt. Etna. Earth and Planetary Science Letters 308 (1–2), 11–22. Elsevier B.V.

Kahl, M., Chakraborty, S., Costa, F., Pompilio, M., Liuzzo, M., Viccaro, M., 2013. Compositionally zoned crystals and real-time degassing data reveal changes in magma transfer dynamics during the 2006 summit eruptive episodes of Mt. Etna. Bulletin of Volcanology 75 (2), 692.

Kress, V., Ghiorso, M., 2004. Thermodynamic modelling of post-entrapment crystallisation in igneous phases. J. Volcanol. Geotherm. Res. 137, 247–260.

Lin, G., Shearer, P.M., Matoza, R.S., Okubo, P.G., Amelung, F., 2014. Three-dimensional seismic velocity structure of Mauna Loa and Kilauea volcanoes in Hawaii from local seismic tomography. Journal of Geophyiscal Research: Solid Earth 119, 4377–4392.

Lockwood, J.P., Lipman, P.W., 1987. Holocene Eruptive History of Mauna Loa Volcano. US Geol. Surv. Pap Volcanism in Hawaii.

Longpré, M.-A., Klügel, A., Diehl, A., Stix, J., 2014. Mixing in mantle magma reservoirs prior to and during the 2011-2012 eruption at El Hierro, Canary Islands. Geology 42 (4), 315–318.

Lynn, K.J., Garcia, M.O., Shea, T., Costa, F., Swanson, D.A., 2017. Timescales of mixing and storage for Keanakako'i tephra magmas (1500-1820 C.E.), Kilauea volcano, Hawai'i. Contrib. Mineral. Petrol. 172 (76).

Matzen, A.K., Baker, M.B., Beckett, J.R., Stopler, E.M., 2011. Fe-Mg partitioning between olivine and high-magnesian melts and the nature of Hawaiian parental liquids. J. Petrol. 52 (7–8), 1243–1263.

Morgan, D.J., Blake, S., 2006. Magmatic residence times of zoned phenocrysts: introduction and application of the binary element diffusion modelling (BEDM) technique. Contrib. Mineraol. Petrol. 151, 58–70.

Morgan, G.B.V., London, D., 1996. Optimizing the electron microprobe analysis of hydrous alkali aluminosilicate glasses. Am. Mineral. 81, 1176–1185.

Mousallam, Y., Edmonds, M., Scaillet, B., Peters, N., Gennaro, E., Sides, I., Oppenheimer, C., 2016. The impact of degassing on the oxidation state of basaltic magmas: a case study of Kilauea volcano. Earth Planet. Sci. Lett. 450, 317–325.

Müller, A., 2005. The Hapaimamo Flow: A Young Pre-Historic Picritic Lava Flow on Mauna Loa's Southwest Rift Zone. MSc Thesis.. University of Massachussetts, Amherst.

Mutch, E.J.F., Maclennan, J., Shorttle, O., Edmonds, M., Rudge, J.F., 2019a. Rapid transcrustal magma movement under Iceland. Nature Geoscience 12 (7), 569–574. Springer US.

Mutch, E.J.F., Maclennan, J., Holland, T.J.B., Buisman, I., 2019b. Millenial storage for near-Moho magma. Science 365 (6450), 260–264.

Mutch, E.J.F., Maclennan, J., Shorttle, O., Rudge, J.F., Neave, D.A., 2021. DFENS: Diffusion chronometry using finite elements and nested sampling. Geochemistry, Geophysics, Geosystems 22.

Okubo, P.G., Benz, H.M., Chouet, B.A., 1997. Imaging the crustal magma sources beneath Mauna Loa and Kilauea volcanoes. Hawaii. Geology 25 (10), 867–870.

Pankhurst, M.J., Morgan, D.J., Thordarson, T., Loughlin, S.C., 2018. Magmatic crystal records in time, space, and process, causatively linked with volcanic unrest. In: Earth and Planetary Science Letters, 493. Elsevier B.V., pp. 231–241.

Park, J., Morgan, J.K., Zelt, C.A., Okubo, P.G., Peters, L., Benesh, N., 2007. Comparative velocity structure of active hawaiian volcanoes from 3-D onshore-offshore seismic tomography. Earth Planet. Sci. Lett. 259, 500–516.

Poland, M.P., Miklius, A., Montgomery-Brown, E.K., 2014. Magma Supply, Storage, and Transport at Shield-Stage Hawaiian Volcanoes. U.S. Geol. Surv. Prof. Pap. 1801 (2010), 1–52.

Prior, D.J., Boyle, A.P., Brenker, F., Cheadle, M.C., Day, A., Lopez, G., Peruzzo, L., Potts, G.J., Reddy, S.M., Spiess, R., Timms, N.E., Trimby, P.W., Wheeler, J., Zetterström, L., 1999. The application of electron backscatter diffraction and orientation contrast imaging in the SEM to textural problems in rocks. Am. Mineral. 84, 1741–1759.

Putirka, K.D., 2008. Thermometers and Barometers for Volcanic Systems. Rev. Mineral. Geochem. 69 (1), 61–120.

Rae, A.S.P., Edmonds, M., Maclennan, J., Morgan, D., Houghton, B., Hartley, M.E., Sides, I., 2016. Time scales of magma transport and mixing at Kīlauea Volcano. Hawai'i. Geology 44 (6), 463–466.

Rasmussen, D.J., Plank, T.A., Roman, D.C., Power, J.A., Bodnar, R.J., Hauri, E.H., 2018. When does eruption run-up begin? Multidisciplinary insight from the 1999 eruption of Shishaldin volcano. Earth Planet. Sci. Lett. 486, 1–14.

Rhodes, M., 1983. Homogeneity of of lava flows: chemical data for historic Mauna Loan eruptions. J. Geophys. Res. 88, A869–A879.

Rhodes, J.M., 1988. Geochemistry of the 1984 Mauna Loa Eruption: Implications for magma storage and supply. J. Geophys. Res. 93 (B5), 4453.

Rhodes, J.M., 1995. The 1852 and 1868 Mauna Loa picrite eruptions: Clues to parental magma compositions and the magmatic plumbing system. In Mauna Loa Revealed: Structure, Composition, History and Hazards. Geophysical Monograph 92, 241–262.

Roeder, P., Emslie, R., 1970. Olivine-liquid equilibrium. Contrib. Mineral. Petrol. 29 (4), 275–289.

Rowland, S.K., Walker, G.P.L., 1987. Toothpaste lava: Characteristics and origin of a lava structural type transitional between pahoehoe and aa. Bull. Volcanol. 49 (4), 631–641.

Ruth, D.C.S., Costa, F., Bouvet De Maisonneuve, C., Franco, L., Cortés, J.A., Calder, E.S., 2018. Crystal and melt inclusion timescales reveal the evolution of magma migration before eruption. Nat. Commun. 9 (1). Springer US.

Saunders, K., Blundy, J., Dohmen, R., Cashman, K., 2012. Linking petrology and seismology at an active volcano. Science 336 (6084), 1023–1027.

Shea, T., Costa, F., Krimer, D., Hammer, J.E., 2015. Accuracy of timescales retrieved from diffusion modelling in olivine: a 3D perspective. Am. Mineral. 100 (10), 2026–2042.

Sisson, T., Layne, G., 1993. H2O in basalt and basaltic andesite glass inclusions from four subduction related volcanoes. Earth Planet. Sci. Lett. 117, 619–635.

Thomson, A., Maclennan, J., 2013. The distribution of olivine compositions in icelandic basaltic and picrites. J. Petrol. 54 (4), 745–768.

Trusdell, F.A., Lockwood, J.P., 2020. Geologic map of the southern flank of Mauna Loa volcano, Island of Hawai'i. Hawai'i. USGS Scientific Investigations Map 2932-C.

Wieser, P.E., Edmonds, M., Maclennan, J., Jenner, F.E., Kunz, B., 2019. Crystal scavenging from mush piles recorded by melt inclusions. Nature. Communications 10.

Wieser, P.E., Lamadrid, H., Maclennan, J., Edmonds, M., Matthews, S., Iacovino, K., Jenner, F.E., Gansecki, C., Trusdell, F., Lopaka Lee, R., Ilyinskaya, E., 2021. Reconstructing magma storage depths for the 2018 Kilauean eruption from melt inclusion CO2 contents: the importance of vapour bubbles. Geochem. Geophys. Geosyst. 22 (2).